

Microstructure and yielding of a capillary force induced gel

Sameer Huprikar^{1,3}, Saurabh Usgaonkar¹, Ashish K. Lele¹, Ashish V. Orpe^{2,3}

¹ CSIR-National Chemical Laboratory, Pune 411008 India

² Academy of Scientific and Innovative Research (AcSIR), Ghaziabad 201002 India

Received: date / Revised version: date

Abstract We have investigated the rheology and structure of a gel formed from a mixture of non-Brownian particles and two immiscible liquids. The suspension of particles in a liquid undergoes gelation upon the addition of a small content of second, wetting liquid which forms liquid bridges between particles leading to a sample spanning network. The rheology of this gel primarily exhibits a yield stress at low shear rates followed by a linear variation of shear stress at high shear rates. The apparent yield stress extracted from the flow curves increases rapidly with volume fraction of second liquid before saturation, while it exhibits a monotonic increase with increasing particle concentration. Rescaling of the yield stress curves using suitable shift factors results in an empirical expression for the yield stress showing squared dependence on liquid fraction and a rapid increase with particle fraction above a certain value, both combined in a highly nonlinear manner. The microstructural variations with changing secondary liquid content and particle fractions are captured using three dimensional X-ray tomography technique. The microstructure is observed to show increased local compactness with increased liquid content and increased spatial homogeneity with increased particle fractions. The images from X-ray tomography are analysed to obtain the distributions of particle-particle bonds (coordination number) in the system which serve to explain the observed yield stress behavior in a qualitative manner.

1 Introduction

The addition of a very small amount of an immiscible liquid to a suspension of non Brownian hard sphere particles causes the suspension to form a (solid-like) gel even at particle volume fractions lower than 0.1, which typically should exhibit liquid behavior (Kao et al., 1975; Cavalier and Larchè, 2002; McCulfor et al., 2011; Koos and Willenbacher, 2011; Koos et al., 2012; Koos and

Willenbacher, 2012; Koos et al., 2014; Koos, 2014; Heidebaugh et al., 2014; Domenech and Velankar, 2014, 2015). The cause for this gel formation in most cases is attributed to the wetting nature (interfacial contact angle < 90 degrees) of the added secondary liquid with respect to the particle surface in the presence of primary suspending liquid. The second liquid, thus, forms tiny bridges between particles leading to a sample spanning network in the system, called as a pendular state gel (Koos and Willenbacher, 2011). The solid-like behavior arises due to attractive capillary force, comprising of Laplace pressure inside the liquid and surface tension at the liquid-liquid-solid contact line, between the particles which provides resistance to flow for small enough forces and imparts a yield stress to this gel. Such solid like behavior is obtained even if the second liquid is non-wetting (interfacial contact angle > 90 degrees). In that case, particles cluster around the droplets of second liquid causing a sample spanning network which is termed as capillary state gel (Koos and Willenbacher, 2011).

Previous studies have shown these gels to exhibit a non-Newtonian rheology comprising of yield stress (τ_y) at low shear rates ($\dot{\gamma}$) and shear thinning behavior at high shear rates (Kao et al., 1975; McCulfor et al., 2011; Koos et al., 2012; Domenech and Velankar, 2015). The yield stress represents solid-to-fluid transition (Bonn et al., 2017; Coussot and Ancey, 1999) while shear thinning behavior represents a decrease in viscosity (η) with increasing shear. For gels arising primarily due to pendular bridging between particles, the capillary attractive force between two particles, separated by distance s , can be expressed by following equation similar to that for wet, cohesive granular materials (Herminghaus, 2005; Strauch and Herminghaus, 2012)

$$F_c = \frac{2\pi R\Gamma \cos \theta}{1 + 1.05\bar{s} + 2.5\bar{s}^2} \quad (1)$$

where, R is the particle radius, Γ is the surface tension of the added liquid, θ is the contact angle made by the liquid with the particle surface, $\bar{s} = s\sqrt{R/V_{sl}}$ is

the normalised separation between particle surfaces and V_{sl} is the liquid bridge volume. The capillary force for particles with negligible separation (i.e. particles touching each other) is given by the well-known expression $F_c = 2\pi R\Gamma \cos \theta$ (Herminghaus, 2005). The macroscopic yield stress, incorporating the particle contact distribution and number of particles per unit volume, is given as (Pietsch and Rumpf, 1967; Schubert, 1984)

$$\tau_y = f(\phi_p)g(\overline{V_{sl}}) \left(\frac{2\pi\Gamma \cos \theta}{R} \right) \quad (2)$$

where, R is the particle radius, $f(\phi_p)$ is a function of particle volume fraction and $g(\overline{V_{sl}})$ is a function of the normalised liquid bridge volume ($\overline{V_{sl}} = V_{sl}/R^3$) and can be expected to have a constant value for a specified liquid fraction. The yield stress values obtained through stress ramp experiments by Koos et al. (2012) for varying temperatures scaled reasonably well with eq. (2), but by assuming $f(\phi_p) \approx \phi_p^2$ as suggested previously for very low volume fraction systems (Pietsch and Rumpf, 1967). Particles of different types and in the diameter range of 1 – 20 microns were employed in this work. The value of Γ was taken to be the interfacial tension between two liquids and the two liquid contact angle $\cos \theta$ calculated using the surface tension of individual liquids. A power-law dependence of yield stress on particle fraction, but with an exponent of 3.3, was also observed by Domenech and Velankar (2015) for studies over a much wider range of volume fractions of silica particles of 2 micron diameter. The yield stress in their work was obtained by fitting the well-known Herschel-Bulkley constitutive equation to the steady shear rheology data. Using stress ramp experiments, Cavalier and Larchè (2002) obtained a power-law dependence of yield stress on particle fraction with an exponent of 4.6 using calcium carbonate particles of sub-micron size. The gelation mechanism in their study was attributed to hydrogen bonding which was later on shown to arise due to capillary forces (Koos and Willenbacher, 2011).

The magnitude of yield stress in several studies exhibits a rapid increase with liquid content followed by a very slow increase (Cavalier and Larchè, 2002; Koos and Willenbacher, 2011; Koos et al., 2012; Dittmann and Willenbacher, 2014; Domenech and Velankar, 2015; Bossler et al., 2018) and then a decrease at even higher secondary liquid content (Koos and Willenbacher, 2011; Koos et al., 2012; Domenech and Velankar, 2015). A similar dependence on secondary liquid content, but for the shear viscosity, was observed previously by McCulfor et al. (2011) using glass spheres of 40 micron diameter. In a recent theoretical study (Danov et al., 2018; Georgiev et al., 2018), the function $g(\overline{V_{sl}})$ in eq. (2) was expressed in terms of the balance between inter-particle capillary attractive and electrostatic repulsive forces. The theory also exhibited a power-law dependence of the yield stress on particle fraction with an exponent of 0.66 and was

shown to agree with experimental results for 4 micron diameter particles.

Unlike the rheology studies which are quite substantial in number, studies about the microstructural details of the gel systems are relatively few and quite sporadic. The formation of the most stable structures for a capillary state gel was modeled by Koos and Willenbacher (2012) using optimisation codes for varying secondary liquid content and contact angles. The increase and subsequent saturation of yield stress with increase in liquid content was attributed, respectively, to the presence of tetrahedral and octahedral clusters in the system. Using confocal imaging, Bossler and Koos (2016) investigated the effect of contact angle (wettability) on the microstructure for solid as well as porous particles. The transition from pendular bridging to a capillary state gel was observed to shift to higher contact angles (> 90 degrees) due to particle porosity. The microstructural differences between capillary state and pendular state gel were quantified using the pair distribution functions computed from acquired images.

In an another study, Fortini (2012) used Brownian dynamics simulations to obtain the evolution of the sample spanning network for a capillary state gel starting from the formation of clusters to the eventual percolation of these clusters. The fractal dimension (d_f) in their work was found to vary from 1.08 ± 0.05 for initial cluster growth to a higher value of 2.6 ± 0.1 corresponding to the random aggregation of very large sized clusters. The structural changes for a pendular state gel, formed using particles of size 2 micron diameter, were visualised using confocal microscopy by Domenech and Velankar (2015). The images showed the presence of percolated pendular structure at lower liquid contents and that of large aggregates at larger liquid contents. Using the observed power-law behavior of yield stress on particle volume fraction and de Gennes scaling concept for polymer gels, Domenech and Velankar (2015) obtained the fractal dimension of their silica particle gel to be 1.79, which is close to that observed for diffusion limited aggregation (Lu and Weitz, 2013). In a very recent study, Bossler et al. (2018) obtained a range of values for fractal dimension (1.9 – 2.8) using rheological scaling laws and confocal imaging for particles in the size range 0.5 microns to 3 microns. The varied range of the values of fractal dimension were attributed to the different lengthscales of the microstructure probed by individual method, thereby, rendering non-uniqueness to the fractal dimension in capillary gel systems. The fractal dimension, however, showed a monotonic increase with particle size, suggestive of increasing compactness in the gel system.

All the prior work presented above exhibits a reasonable body of work available for capillary force induced gels, but centered around particle sizes closer to the colloidal range. The primary intention of this work is to extend the capillary gel literature to much larger par-

Table 1 Physical properties of liquids used for gel preparation. CHB: Cyclohexyl bromide, DEC: Decahydronaphthalene, TG: Thioglycerol and 1P: 1 propanol. The viscosities and surface tensions were measured, respectively, using rheometry and pendant drop method. The interfacial tension between the two liquid mixtures, CHB-DEC and TG-1P was measured as 3.36 mN/m. The static contact angle of TG-1P mixture on PMMA surface in the presence of CHB-DEC liquid was measured as 58 ± 2.5 degrees (see text for more details)

Liquid	Density (g/cc)	Viscosity (mPa s)	Refractive Index	Surface tension (mN/m)
CHB	1.33	2	1.495	29.9
DEC	0.89	2	1.481	30.3
TG	1.25	137	1.527	50.5
1P	0.80	2	1.384	22.8

ticle size ranges (few hundred microns), closer towards those typically observed for the wet granular materials, which has not been done previously. The primary reason for using larger particles is to allow for much easier visualisation and quantification of the gel microstructure, which has not been explored significantly in the literature and which is absolutely necessary to understand the bulk rheology behavior. Secondly, this allows for the theoretical advancement of the subject from the granular matter perspective as well. The larger sized particles would also preclude the Brownian motion responsible to some extent for ageing, thereby simplifying the rheology measurements (Moller et al., 2009; Joshi and Petekidis, 2018) and also reduce the difficulties in measuring microstructural details due to possible particle motion. While weaker gels are expected with increased particle sizes (Koos et al., 2012; Bossler et al., 2018), the carryover of the entire rheology behavior to gels formed for large sized particles is not clear, which includes the dependence of yield stress on particle and secondary liquid content. The rheology behavior of the system studied over here reveals the presence of a yield stress at low shear rates followed by a linear increase of shear stress at large shear rates. Using suitable scaling analysis it is shown that the yield stress exhibits a non-linear dependence on particle and secondary liquid content. The three dimensional visualisation of the microstructure using laser imaging and X-ray tomography and subsequent quantification of the microstructure using image analysis serves to explain the qualitative nature of the yield stress behavior in a reasonable manner.

2 Experimental details

The suspension comprises of three constituents: (i) polymethyl methacrylate (PMMA) particles, purchased locally, of mean diameter $D = 350 \pm 50$ microns as mea-

sured by imaging and analysis of several hundred particles (ii) a primary suspending liquid made from a mixture of two liquids, viz., Cyclohexyl bromide (CHB) procured from Spectrochem and Decahydronaphthalene (DEC) procured from Otto Chemicals and (iii) secondary liquid also made from a mixture of two liquids, viz., Thioglycerol (TG) procured from Sigma-Aldrich and 1-Propanol (1P) procured from Thomas Baker. The physical properties for all the four liquids are provided in Table 1.

The liquids, both, primary and secondary, were chosen such that (i) the secondary liquid is wetting with respect to particle surface in presence of primary liquid (ii) the densities and refractive indices of the both liquids are same as that of the particles. A perfect density matching is needed to prevent the particles from settling/floating in the suspending liquid (note the particles are quite large in size while liquid viscosities are quite low). Particle settling or floating leads to (i) undesired phase separation between particles and liquids, which may hinder the preparation of the gel and (ii) incorrect interpretation of the rheology data of the suspension due to possible phase separation. An accurate refractive index matching is needed for visualisation in the bulk. It also helps in ascertaining the accurate matching of density between particles and liquid mixtures as explained later. The density of the particles and liquids was matched to the order of 3 – 4 decimal places, while the refractive indices of particles and liquids was matched to make the suspension transparent enough to visualize 20 – 30 particle diameters inside the sample. The details of refractive and density matching is provided in A.4.

The wetting ability of TG-IP mixture with respect to the particle surface was measured in terms of the contact angle made by its drop on a PMMA plate (of same material as particles) in presence of surrounding CHB-DEC mixture. The drop was placed on a horizontal PMMA plate immersed in CHB-DEC mixture and was imaged by a camera placed sideways and in the plane of the plate (see fig. 1a). The images were analysed using ImageJ software to obtain the static contact angle. The reported value of the contact angle in Table 1 represents an average over ten independent measurements. Given the value of the measured contact angle, it is expected that the TG-IP mixture, when added as a secondary liquid to the suspension of PMMA particles in CHB-DEC mixture, will form a gel arising out of pendular bridging between particles (as clearly evidenced in fig. 1b and fig. 7). Corresponding description is provided in section 3.3).

Stress ramp measurements were carried out for every gel sample using concentric cylinder (cup-bob) assembly in the stress controlled MCR-301 rheometer (Anton Paar Inc.). Given the large particle size employed, the outer cylinder of larger radius (11.33 mm) was fabricated separately to employ shearing thickness (3 mm) of about 8–9 particle diameters given the radius of the rotating bob to be 8.33 mm. In all the experiments the temperature

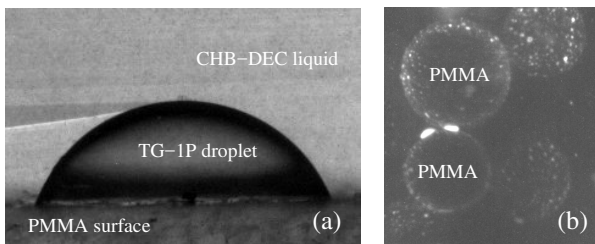


Fig. 1 (a) Contact angle formed by a drop of TG-1P mixture on the PMMA surface in presence of surrounding CHB-DEC mixture. (b) Formation of (TG-1P mixture) liquid bridge between two PMMA particles as well as droplet on particle surface in bulk CHB-DEC mixture. Two dimensional image about 5 particle diameters away from the walls, obtained by fluorescing the secondary liquid using laser sheet. (See text for more details)

within the rheometer was maintained at 25 ± 1 deg C. Instead of preparing the sample and then transferring to the rheometer, the sample was prepared in the detachable cylinder (cup) itself. Initially, a pre-determined quantity of particles was added to the primary liquid (CHB-DEC mixture) and stirred for about 10 minutes. A known, tiny quantity of secondary liquid (TG-1P mixture) was then added to the suspension and the entire mixture was stirred again for another 10 minutes. This second stirring yielded a gel-like material whose strength and characteristics are expected to depend on the quantity of particles and secondary liquid added. It is anticipated that the stirring of the mixture generates several microdroplets from the secondary liquid which leads to formation of the gel. Particle volume fraction (ϕ_p), was varied from 0.1 to 0.4, while secondary liquid volume fraction (ϕ_{sl}) was varied from 0.001 to 0.025. The volume fraction of an entity (particle or liquid) was obtained as the ratio of its volume to the total volume comprising of both the liquids and particles. The cylinder was then assembled back in the rheometer. The gel was first rapidly sheared at 100 1/s for 2 minutes to break down the gel completely to a sol state having a very low viscosity. The sample was then allowed to recover under quiescent conditions for 20 minutes (minimal stress applied for five minutes followed by no stress for fifteen minutes) till the viscosity increases significantly and reaches a constant value. This attainment of the constant viscosity value represents the initial state of the gel and the methodology, thus implemented, allows for complete removal of any preparation history. The gel was then subjected to stress ramp measurements, wherein the stress was increased in stepwise manner over the entire range. The shear rate was recorded at each stress after 10 seconds of acquisition time (t_{aq}). A few experiments were also done for $t_{aq} = 100$ seconds and $t_{aq} = 1000$ seconds. In essence, each step is a creep experiment over the acquisition time. The magnitude of applied stress was varied over four orders of magnitude with the corresponding

measured shear rate varying over eight orders of magnitude. It should be noted that the formation of the droplets of secondary liquid, hence the gel, is sensitive to the preparation protocol which includes the constituent addition sequence as well as the stirring speed of the mixture. The change in the protocol, thus, may alter the observed rheology and the underlying microstructure as shown previously (Domenech and Velankar, 2014; Yang and Velankar, 2017).

The three dimensional microstructural details of the gel were obtained using X-ray tomography (Zeiss XRadia 510 Versa, X-ray microscope). A small amount (about 1.5 ml) of gel sample (obtained after stirring as mentioned above) was transferred to a polypropylene microcentrifuge tube (volume 2.5 ml), which was carefully placed on the sample holder to ensure centralised positioning. The assembly was placed in the path of a polychromatic X ray beam and rotated by 360 degrees. An image of the gel sample (approximately 20×20 particle diameters) was acquired every 1.2 degrees of rotation at an exposure time of 10 seconds per image. The three dimensional reconstruction of all images (region spanning $20 \times 20 \times 20$ particle diameters) was then analysed using standard IDL routines to obtain the centroid and radius of every particle (procedure described in section 3.3) which were further used to determine relevant structural information in the system.

3 Results and Discussion

The behavior of the flow curves (stress vs shear rate) obtained from step-wise stress ramp rheology is discussed first. The value of the yield stress for different cases is obtained from the flow curves and its dependence on variation of ϕ_p and ϕ_{sl} is discussed next. This is followed by simple scaling analysis (data shifting) to obtain an empirical expression for the yield stress in terms of ϕ_p and ϕ_{sl} . We, then, discuss the microstructural details of the gel as acquired using three dimensional X-ray tomography technique and provide some quantitative measurements to try and explain the yield stress behavior.

3.1 Stress ramp rheology

Figure 2 shows the variation of shear stress (τ) with shear rate ($\dot{\gamma}$) for varying values of ϕ_{sl} and ϕ_p . The error bars, shown for a few profiles (corresponding to the images shown in fig. 6), represent the standard deviation over 6 – 7 independent measurements. Without the addition of secondary liquid ($\phi_{sl} = 0$), a linear behavior is observed throughout as would be expected for the shearing of a dilute suspension of hard spheres (Stickel and Powell, 2005). The addition of tiny amounts of secondary liquid induces non-linear behavior (see fig. 2a,b).

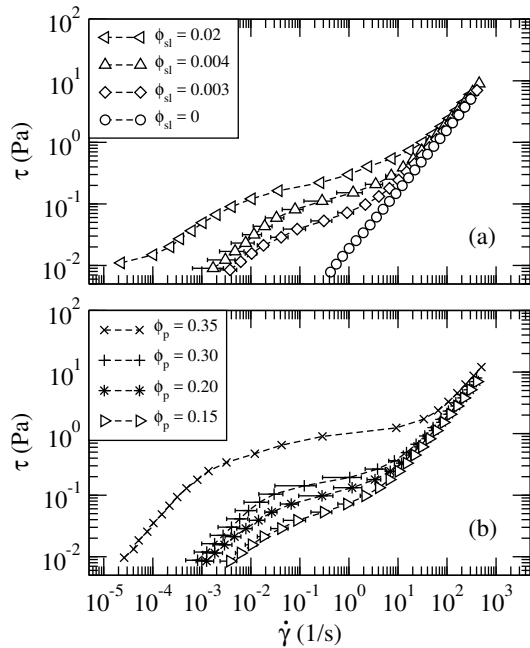


Fig. 2 Stress ramp rheology data. (a) Experimental data for $\phi_p = 0.15$ (b) Experimental data for $\phi_{sl} = 0.003$. Every curve shows three distinct flow regimes (see text for more details)

A continuous increase in the shear stress value is observed over 7 – 8 orders of magnitude variation in shear rates.

When subjected to very high shear rates ($\gg 10s^{-1}$), the gel structure is expected to break, thereby reducing it predominantly to a binary system of particle and primary suspending liquid, with interspersed secondary liquid droplets. The flow curve should then exhibit a behavior similar to that of a binary particle-primary liquid suspension. All the flow curves for constant ϕ_p and varying ϕ_{sl} (see fig. 2a), merge onto the curve for $\phi_{sl} = 0$ at higher shear rates, thus indicating a linear behavior for all cases with nearly similar viscosity values (η_∞). The flow curves for constant ϕ_{sl} and varying ϕ_p (see fig. 2b) also merge onto one curve at higher shear rates, again suggesting linear behavior and constant viscosity. However, the viscosity values are slightly different in each case, corresponding to the values of ϕ_p , but are not clearly discernible due to closeness of the data on a log-log plot. The viscosity values measured separately for a binary suspension (no secondary liquid) show a very slow increase with increasing ϕ_p till 0.4 beyond which they increase rapidly.

For the lower shear rate range ($10^{-2}s^{-1}$ to $10s^{-1}$), the shear stress shows a very slow variation with shear rate (plateau or shoulder formation in the flow curves). This represents the yield stress part of the curve. Previous studies for very small particle sizes have observed flow curves exhibiting two regions, viz. a true yield stress followed by shear thinning behavior (Herschel-Bulkley model) using polymeric primary as well as secondary liq-

uids (Domenech and Velankar, 2015) and an ideal Bingham flow behavior using Newtonian liquids (Kao et al., 1975).

The absence of true yield stress type behavior observed in fig. 2 is most likely due to the smaller acquisition time ($t_{aq} = 10$ seconds) used in the stress ramp experiments. For $t_{aq} = 100$ and $t_{aq} = 1000$ seconds, a more pronounced plateau is observed. The flow curves below this plateau shift to much lower shear rates than those observed for $t_{aq} = 10$ seconds. This behavior is shown for one case, $\phi_p : 0.20$ and $\phi_{sl} : 0.003$, in fig. 3b. Similar qualitative behavior is observed for all other cases studied. A rightward shift, towards higher shear rates, is also observed, though the effect saturates with increasing values of t_{aq} . The magnitude of the yield stress, however, does not change with the change in acquisition time. The observed behavior suggests that the non-Brownian suspensions studied in this work are likely to exhibit true yield stress and discontinuous flow curve, but only for large enough acquisition times.

The observed increase of shear stress with shear rates, below the yield stress, can be attributed to subtle rearrangements within the gel microstructure, which may be transitory in nature given the dependence on acquisition time. It is, thus, not surprising that flow curves, below the yield stress, are different from each other for varying combinations of particle and secondary liquid content used.

With a view to further explore the nature of the gel, particularly below yielding, the strain experienced by the sample was measured for each stress value over a particular acquisition time used. The variation of the applied stress with the realised strain and pertinent description is provided in A.2. The reasonable superposition of the data for different acquisition times below the yielding is suggestive of a possible elastic deformation of the gel which is conspicuously absent for stresses above yielding. The strain itself, however, increases with time for stresses above as well as below yielding (see the description and corresponding figure in A.3). The increase in strain represents plastic deformation of the sample in consideration. The complicated rheology, so observed, for the gel below the yielding will require further investigation which is not within the scope of present work.

To elucidate the possible effect of wall slip and confinement on the rheology results, a few measurements were carried out in the separately fabricated outer cylinder of larger radius (14.33 mm) resulting in a larger shearing thickness (6 mm), about 18 – 20 particle diameters wide. The rheology data and the corresponding discussion for two shearing gaps is provided in A.1. The results suggest that the overall rheology behavior does not seem to be qualitatively affected by the shear gap and due to the presence of a small amount of possible wall slip. Our primary interest is to understand the yield stress behavior and its dependence on the microstructure (presented in section 3.3). The remainder of the discus-

sion refers to the data acquired in 3 mm shearing gap and for an acquisition time (t_{aq}) of 10 seconds.

Given the absence of easily discernible yield stress in the flow curves shown in fig. 2, it is not possible to fit a Bingham constitutive equation to obtain the yield stress value. We, instead, make use of the following phenomenological stress constitutive equation proposed by Papanastasiou (1987), which has been used significantly for modeling studies of polymeric systems (Mitsoulis, 2007)

$$\tau = \tau_y [1 - \exp(-A\dot{\gamma}^q)] + \eta_\infty \dot{\gamma} \quad (3)$$

where, τ_y represents the yield stress, η_∞ represents the Newtonian viscosity and $\dot{\gamma}$ represents the shear rate. For $A = 0$, the equation for Newtonian liquid is recovered, while for $A \rightarrow \infty$, the model is same as the ideal Bingham visco-plastic model. The parameters A and q are adjusted to obtain the best fit to the data. We do not observe any specific trend in the values of A and q , the values for which are, thus, not reported over here. We wish to stress here that the use of eq. (3) is done purely for the sake of mathematical fitting in order to extract a value of yield stress from the flow curve data. By using eq. (3) we do not mean to imply that the flow of the suspensions can be physical modeled by the Papanastasiou constitutive equation. Indeed, the time dependent stress response in the very low shear region is not captured by eq. (3). A more complex constitutive relation will be required to capture the elasto-viscoplastic character of the suspension described in A.2 and A.3 which is not within the scope of the present work. The fit of eq. (3) to the data is shown for a few cases in fig. 3, which is representative of fits obtained for all the data. The yield stress (τ_y) obtained from data fitting shows interesting and rich behavior which will be discussed next.

3.2 Yield stress behavior

The variation of yield stress with the ratio ϕ_{sl}/ϕ_p is shown in fig. 4 for the entire range of ϕ_{sl} and ϕ_p investigated in the experiments. The error bars shown for a few cases (corresponding to the images shown in fig. 6) represent the standard deviation of the yield stress values obtained by fitting the model (eq. (3)) to 6–7 independent stress ramp flow curves. They also correspond to those cases for which the microstructure was studied in detail (described in section 3.3). Four different behaviours are evident from the figure. The yield stress of the gel first increases rapidly with increasing ϕ_{sl} at constant ϕ_p before saturating at higher values of ϕ_{sl} (fig. 4a). On the other hand, the yield stress of the gel also increases monotonically with increasing ϕ_p at constant ϕ_{sl} (fig. 4b). However, saturation of yield stress values is not observed, but the data is suggestive of a rapid rise in the yield stress beyond certain value of ϕ_p . Thirdly, for a fixed value of ϕ_{sl}/ϕ_p (simultaneous increase in ϕ_p and ϕ_{sl}), the yield stress shows a continuous increase (traversing vertically

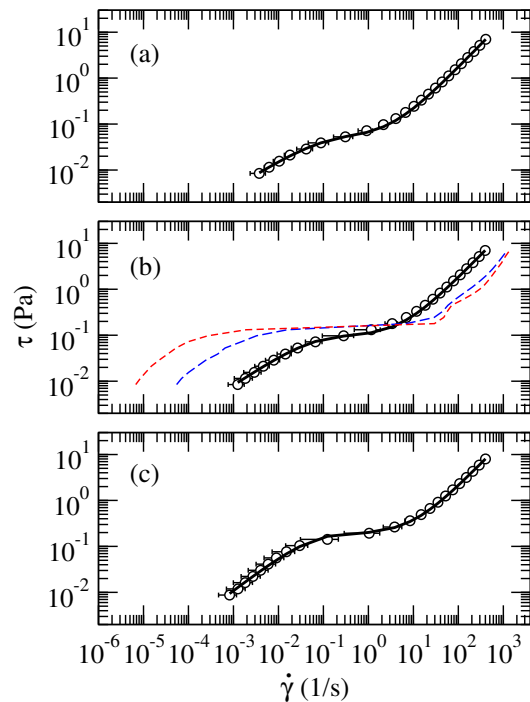


Fig. 3 Fitting of the Bingham-Papanastasiou model (see text for details) with the stress ramp rheology data obtained for $\phi_{sl} = 0.003$ and (a) $\phi_p = 0.15$ (b) $\phi_p = 0.20$ (c) $\phi_p = 0.30$. The dashed blue and red lines in (b) represent data for longer acquisition times (t_{aq}) of 100 s and 1000 s, respectively. (See text for more details)

upwards in fig. 4a and b). And finally, a constant value of yield stress (τ_y) is observed with varying ϕ_{sl}/ϕ_p achieved either by simultaneous increase in ϕ_{sl} and decrease in ϕ_p or vice-versa (traversing horizontally in fig. 4a and b). For all the values of ϕ_{sl}/ϕ_p lower than those reported in the figure, a much weaker gel is obtained for which the rheometer response is not accurate enough to obtain the flow curves. The above discussion is highly suggestive of a non-linear dependence of yield stress on ϕ_{sl} and ϕ_p . We, next, carry out a scaling analysis of the data to recover this non-linear dependence.

The yield stress curves for constant ϕ_p (fig. 4a) are shifted vertically and horizontally, using respective shift factors, s_1 and s_2 to obtain reasonable collapse of the data as shown in fig. 5a. The variation of these shift factors with ϕ_p is shown in fig. 5b and 5c. Fitted (dashed) lines to the data for shift factors yields $s_1 \propto (1/\phi_p - 2.5)^{-1}$ and $s_2 \propto 1/\phi_p$. Substituting these expressions for s_1 and s_2 in the power-law model fit (of exponent 2) to the yield stress data (shown as dashed line in fig. 5a), provides the non-linear dependence of the yield stress on ϕ_{sl} and ϕ_p given as $\tau_y \propto \phi_{sl}^2 (1/\phi_p - 2.5)^{-1}$. This power-law fit is, however, not valid at higher values of ϕ_{sl}/ϕ_p for which the yield stress shows saturation and remains nearly constant. In a similar vein, horizontal and vertical shifting of the yield stress data for constant ϕ_{sl} (fig. 4b) results in the same scaling, namely

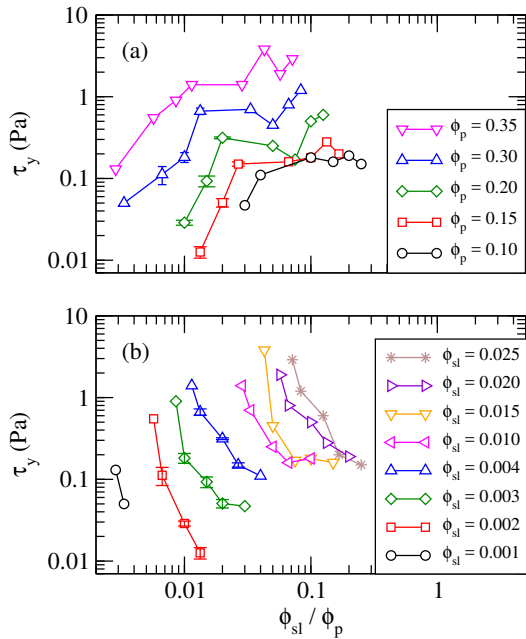


Fig. 4 Variation of yield stress (τ_y) with the ratio ϕ_{sl}/ϕ_p . (a) Data for constant values of ϕ_p and varying values of ϕ_{sl} . (b) Data for constant values of ϕ_{sl} and varying values of ϕ_p .

$\tau_y \propto \phi_{sl}^2 (1/\phi_p - 2.5)^{-1}$, thus confirming the consistency of data shifting and scaling. The variations of shift factors, m_1 and m_2 , are shown in fig. 5e and 5f, respectively, while the final scaling is shown as dashed line in fig. 5d. It is also possible to fit an equation comprising of an exponential term (not shown) to the entire range of data (increasing as well as plateau region) from fig. 5a and 5e instead of the power-law fit in the increasing region of τ_y . Subsequent simplification after model fitting yields an alternate expression for the yield stress given as $\tau_y \propto [1.0 - \exp(-k\phi_{sl}^2)](1/\phi_p - 2.5)^{-1}$, where k is a numerical constant. Assuming pendular state gels with liquid bridging between particles, it is expected that the yield stress would scale with Γ/R in accordance with eq. (2) as also observed previously (Koos et al., 2012). This scaling behavior, however, cannot be verified as the particle size and liquids were not varied in the experiments. We, next, discuss the dependence of yield stress on secondary liquid fraction and particle volume fraction.

The shifted data in fig. 5a shows a rapid increase of yield stress followed by a very slow increase with increasing ϕ_{sl} for a fixed value of ϕ_p . This behavior is in agreement with previous experimental observations for such gel systems (Kao et al., 1975; Koos and Willenbacher, 2011; Koos et al., 2012; Dittmann and Willenbacher, 2014; Domenech and Velankar, 2015; Bossler et al., 2018) as well as for cohesive granular systems (Scheel et al., 2008). The increasing yield stress region is generally referred to as the pendular regime while the region corresponding to very slow increase is referred as the funicular regime characterised by coalescence of liquid bridges (Her-

minghaus, 2005; Domenech and Velankar, 2015; Bossler et al., 2018). The yield stress corresponds to the effective force required for rupturing the weakest attractive (physical) bonds between particles in the gel resulting in a shear plane along which the material yields. We conjecture that the increase in the yield stress with increasing secondary liquid for fixed particle content originates out of two possibilities, viz., due to more number of particle-particle (physical) bonds formed with added liquid and possible increase in the volume of liquid bridge between particles (which is, however, not possible to quantify with the available experimental set-up). The predominant presence of the latter has been shown recently by Weis et al. (2019) using tomography measurements with millimeter sized particles and a completely wetting liquid. The increased liquid bridge volume should increase the capillary attractive force between particles (see eq. (1)) provided the gel state is in the pendular regime (Willet et al., 2000; Herminghaus, 2005) which the data seems to correspond to and will require a larger separation distance to be achieved before breaking of the particle-particle bonds as observed previously (Willet et al., 2000; McCulfor et al., 2011; Pitois et al., 2000). The squared dependence on liquid content as seen in fig. 5a, e or the alternate expression comprising of an exponential term specified above has not been observed before. The explanation will, perhaps, require a relation between liquid bridge volume and added secondary liquid content (specific expression for $g(\bar{V}_{sl})$ in eq. 2), which we are unable to provide at the moment. Such a relation exhibiting a one-third dependence of liquid bridge volume on the ratios of the volume of secondary liquid to particle content has been proposed previously (Kao et al., 1975) with the yield stress eventually showing a power-law behavior having exponent $1/3$ with increasing ϕ_{sl}/ϕ_p . For a significant increase in the liquid content beyond that corresponding to saturation, the yield stress has been shown to exhibit a continuous decrease (not studied in this work) (Kao et al., 1975; Koos and Willenbacher, 2011; Dittmann and Willenbacher, 2014; Domenech and Velankar, 2015; Bossler et al., 2018).

An increase in the yield stress is also observed with increasing ϕ_p for constant ϕ_{sl} as seen from the shifted data in fig. 5d. However, the behavior suggests a rapid increase occurring around $\phi_p = 0.4$ as obtained from the fitted equation. Increase in the number of particles present in the gel corresponds to increased number of attractive physical bonds formed between particles, thereby leading to higher yield stress. However, given that liquid content is maintained the same, larger number of bonds are, perhaps, formed either by more optimal usage of the existing liquid or due to excess liquid droplets in the system which were never used in the network, the latter case being more probable (see fig. 7). The effect of increased crowding at larger ϕ_p supposedly supplements the capillary bridging induced particle connectivity making the gel that much harder to shear

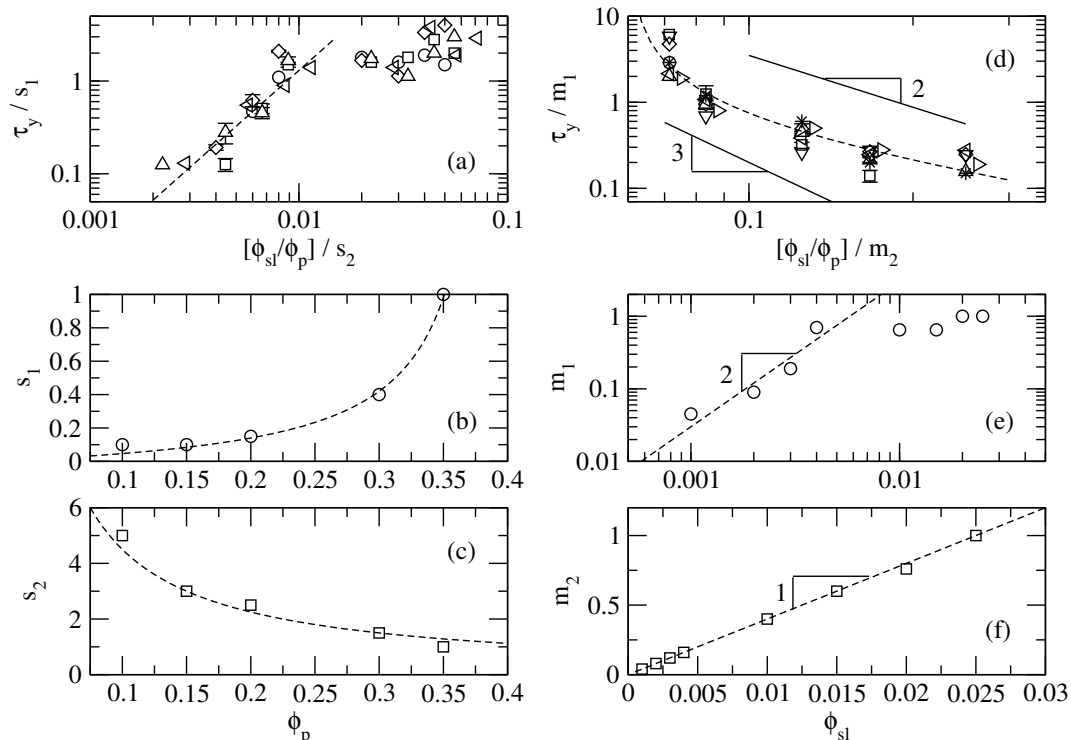


Fig. 5 Scaling analysis. Shifting of the yield stress data for varying values of ϕ_{sl}/ϕ_p ratio obtained at (a) fixed values of ϕ_p and (d) fixed values of ϕ_{sl} . The error bars are shown in (a) and (d) for a few cases, the same as those in fig. 4. (b, c) Variation of scaling factors s_1 and s_2 with ϕ_p , respectively. (e, f) Variation of scaling factor m_1 and m_2 with ϕ_{sl} , respectively. Dashed lines show specific equation fits to the data (see text for details). Solid lines in (d) represents power-law variation with exponents 2 and 3 (see text for more details)

thereby showing a faster increase in the yield stress. The precise value of 0.4 is, however, the result of the fitting to the experimental data over the limited range of ϕ_p values studied over here. Overall, the dependence of the yield stress on particle fraction is stronger compared with that on the secondary liquid content.

Figure 5d also shows a power-law dependence of τ_y on ϕ_p with two different exponents. The power-law variation with exponent 2 agrees with previous predictions (Kao et al., 1975; Pietsch and Rumpf, 1967). The power-law fit with exponent 3.3 as observed by Domenech and Velankar (2015) and that with an exponent value around 4, as recently reported by Bossler et al. (2018) however seems to agree only for the higher range of ϕ_p . The observed discrepancy with our experimental results over the entire range of ϕ_p studied can be attributed partly to the differences in the type of flow curves observed in different studies and partly to the very large particles used (hence weaker gels) for our system. An even higher value of power-law exponent (4.6) has been observed for a gel considered to be arising out of hydrogen bonding (Cavalier and Larchè, 2002), but later on shown to be actually arising due to capillary bridging (Koos and Willenbacher, 2011). We also note recent theoretical and simulation study for particles with attractive forces which have shown such power-law dependence with ex-

ponents 3.5 and 3.9, respectively, but for a compressive yield stress (Roy and Tirumkudulu, 2016).

3.3 Gel microstructure

The three dimensional reconstructed images (from a perspective view angle) for a few cases, as obtained from X-ray tomography technique, are shown in the fig. 6. A similar diagram, but only schematically, was proposed previously (Domenech and Velankar, 2015) to emphasise, qualitatively, the observed bulk rheology behavior. All images represent the values of particle to liquid volume ratios over which the yield stress varies and has not saturated to a constant value. Each image represents a 3D slice of size $20 \times 20 \times 10$ particle diameters, while the movies corresponding to each of these images (of a larger region $20 \times 20 \times 20$ particle diameters) are available as supplementary material. A thinner slice is included over here for ease in visualisation of the three dimensional structure. As seen from the figure, each image clearly depicts a particular microstructure for specified ϕ_{sl} and ϕ_p corresponding to a different yield stress (τ_y). The variation of ϕ_{sl} , ϕ_p , their ratio and τ_y is clearly shown in the figure and is in accordance with the data shown in fig. 4.

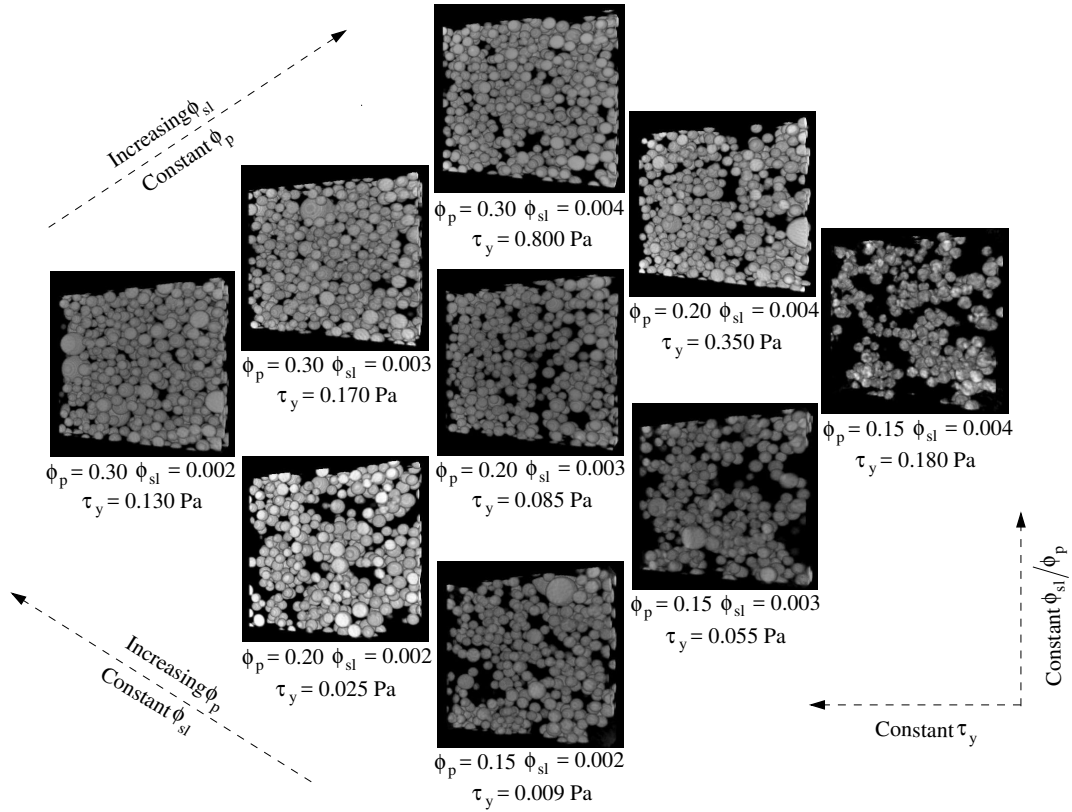


Fig. 6 X-ray tomography images exhibiting the microstructure obtained for varying values ϕ_{sl} and ϕ_p . The yield stress value corresponding to each microstructure are also mentioned in the figure (see text for more details about tomography measurement)

The detailed view of the distribution of the secondary liquid (TG-1P mixture) in the gel matrix for three specific cases is shown in fig. 7. A thin laser sheet illuminates a plane in the bulk (about 10–15 particle diameters from end walls) of the sample placed in a transparent walled rectangular cell and fluorescing the dye present in the secondary liquid to generate the two dimensional images shown in the figure. The un-dyed bulk liquid and the particles are not visible due to very good refractive index matching achieved. The particle presence is, however, perceived from the bright circular rings which represent secondary liquid droplets accumulating around the particle. A very bright puddle represents a very large drop of secondary liquid, perhaps not effectively broken into small micro-droplets during sample preparation. Note that not every drop of secondary liquid participates in particle bonding/connectivity in the sample. However, those participating do form liquid bridges connecting two or more particles as exhibited in the closer view shown in fig. 7c. In this scenario, the exact amount of the secondary liquid involved in liquid bridging cannot be estimated. Nevertheless, increased content of secondary liquid, measured as ϕ_{sl} , does show a direct correlation with increasing and saturating yield stress.

The image matrix shown in fig. 6 suggests four key microstructural behaviours. Increasing value of ϕ_{sl} for

fixed ϕ_p seemingly increases the local porosity, but only slightly. This represents slight rearrangements between particles to form more bonds (more local compactness) while maintaining the base sample spanning structure, responsible for gel behavior. An increase in the porosity value with increasing value of ϕ_{sl} followed by saturation at very high values of ϕ_{sl} (akin to yield stress behavior) has been observed previously, accompanied by qualitative differences in the pore size distribution for different values of ϕ_{sl} (Dittmann and Willenbacher, 2014). Now, keeping the value of ϕ_{sl} fixed while increasing the value of ϕ_p decreases the porosity due to crowding by additional particles which occupy the void space and form more bonds. The yield stress in both cases increases significantly. Varying both quantities simultaneously provides interesting behaviours. A proportionate increase in ϕ_{sl} and ϕ_p to maintain a constant ratio causes increased crowding (more particles, more liquid, more bonding). The yield stress, quite obviously, increases significantly in this case. Finally, increasing ϕ_{sl} and decreasing ϕ_p simultaneously or vice-versa, respectively, increases or decreases microstructural porosity, but interestingly maintains a constant yield stress for the gel system. The yield stress in the latter is through increased crowding (bonding) and in the former case is, perhaps, due to increased liquid bridge volume and slight rearrangement in the mi-

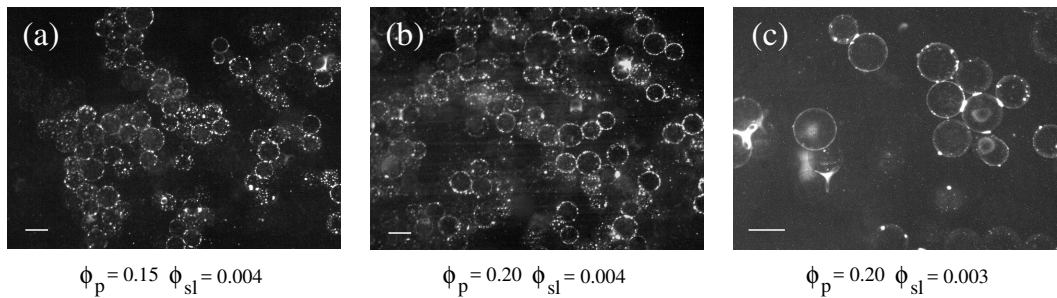


Fig. 7 Two dimensional images providing visual presence/distribution of the secondary liquid within the gel microstructure. Each image is obtained by a laser sheet illuminating a plane away from the walls (in the bulk) and fluorescing the dyed secondary liquid (see text for imaging details). Images in (a) and (b) are representative of the three dimensional matrix obtained by sweeping the laser sheet in the sample. (c) Image showing a much closer view depicting the liquid bridges formed between the particles. The scale bar shown at the bottom left in each figure corresponds to 350 microns.

crostructure. To summarise, a wide range of microstructures are realizable by fine tuning ϕ_{sl} and ϕ_p to achieve the desired strength (yield stress) for the gel system. We next try to explain the observed microstructural and yield stress behavior using some quantitative measurements.

The images obtained from X-ray tomography measurements were analysed using centroid algorithm in IDL (Interactive Data Language), after appropriate filtering and contrast adjustment, to obtain the particle centroids and radius to a pixel accuracy. Given the noise/distortion in the images, about 85% of particles were detected in each sample. This data was then used to determine the particle connectivity in the gel sample. Two particles were considered to be bonded to each other (due to liquid bridge) if the geometric distance d_c between their individual centroids is less than $1.15 (D_1 + D_2)/2$, where D_1 and D_2 are the diameters of two particles. The value 1.15 was fixed to account for the possible errors in centroid and particle radius determination and was arrived at after analysing image sets containing particles of known centroids and radii created manually. The number of bonds associated with every detected particle was obtained using above arguments for each of the nine cases shown in fig. 6. The data, averaged over 2 – 3 experimental runs (tomography sets) for each case, was then used to calculate the distribution $P(n_{bond})$ where, n_{bond} is the number of bonds associated with a particle and $P(n_{bond})$ is the number of particles in the system exhibiting n_{bond} number of bonds. The summation of the values of $P(n_{bond})$ over all values of n_{bond} then corresponds to the average number of particles detected in an image. In the following, the qualitative behavior of the distributions is discussed for three parametric variations, viz. increase in ϕ_{sl} for fixed values of ϕ_p , increase in ϕ_p for fixed values of ϕ_{sl} and increase in both, ϕ_{sl} and ϕ_p , while keeping the ratio ϕ_{sl}/ϕ_p constant.

The value of $P(n_{bond})$ for $n_{bond} = 0$ represents number of particles with no connectivity. This number varies from around 180 (about 10–12% for total particles iden-

tified) for the smallest liquid and particle fraction to around 70 – 80 (about 3.5% of total particles identified) for the largest liquid and particle contents studied. The number arises due to the (i) possibility of individual particles remaining suspended in the gel without connecting to any cluster (ii) possible errors in detecting connected particles and (iii) the inability of the image analysis algorithm to detect all the particles in the system. The relative contribution of these three effects is, however, not possible to quantify.

We next look at the effect of increasing content of secondary liquid for fixed value of ϕ_p . This corresponds to an increase in the ratio ϕ_{sl}/ϕ_p and represents a right-upward travel in fig. 6. The distribution, $P(n_{bond})$, is shown in fig. 8. As discussed earlier, the increased liquid content does visually show a slight change in porosity as noted in fig. 6 while preserving the sample spanning network resulting in a gel-like behavior. This slight change in porosity is not reflected appreciably in the distribution. A slight rightward shift at highest particle fraction is observed in (fig. 8c), which is most likely, due to larger number of particles available for possible rearrangement of the microstructure. The yield stress, however, shows an appreciable change, from 0.009 Pa to 0.18 Pa in case (a), from 0.025 Pa to 0.35 Pa in case (b) and from 0.13 Pa to 0.8 Pa in case (c). The increase in the yield stress can then be attributed primarily to the increase in the liquid bridge volume (discussed earlier in conjunction with eq. (1)) and slight contribution due to increased number of bonds per particle at highest particle fraction (Weis et al., 2019). The exact dependence of liquid bridge volume on ϕ_{sl} as shown previously (Willet et al., 2000; Herminghaus, 2005; Pitois et al., 2000; McCulfor et al., 2011), but for contact angles much smaller than 60 degrees observed over here, is, however, not possible to quantify.

The distribution, $P(n_{bond})$, for increasing values of ϕ_p at fixed values of ϕ_{sl} is shown in fig. 9. The variation represents decreasing value of the ratio ϕ_{sl}/ϕ_p and corresponds to left-upward travel in fig. 6. Unlike previ-

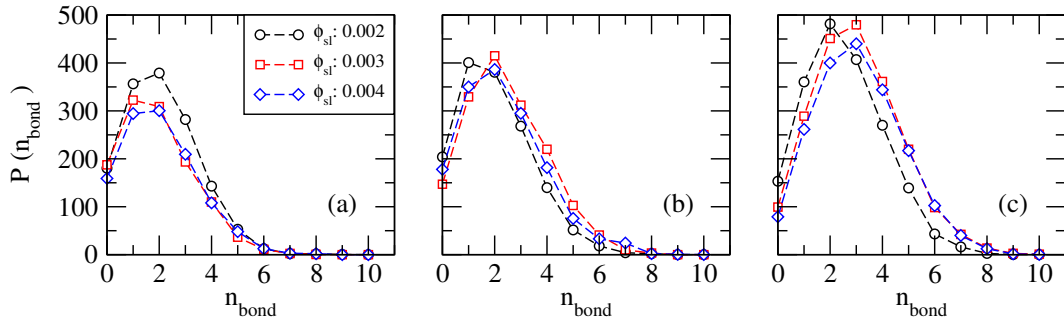


Fig. 8 Variation of the distribution of the number of particles having n_{bond} number of bonds with ϕ_{sl} for (a) $\phi_p = 0.15$ (b) $\phi_p = 0.20$ and (c) $\phi_p = 0.30$.

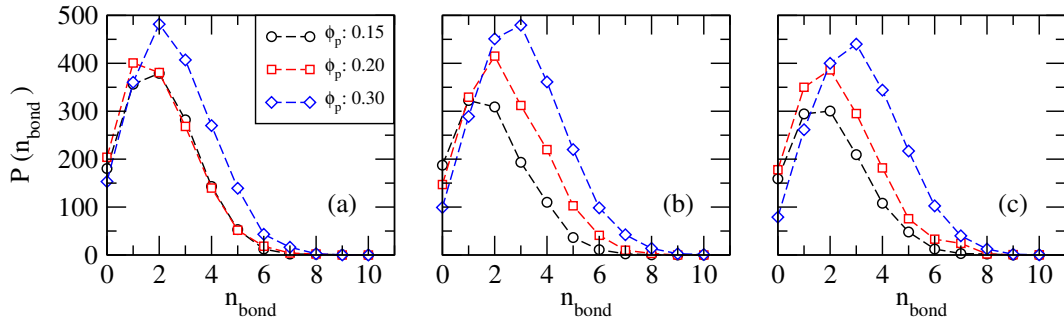


Fig. 9 Variation of the distribution of the number of particles having n_{bond} number of bonds with ϕ_p for (a) $\phi_{sl} = 0.002$ (b) $\phi_{sl} = 0.003$ and (c) $\phi_{sl} = 0.004$.

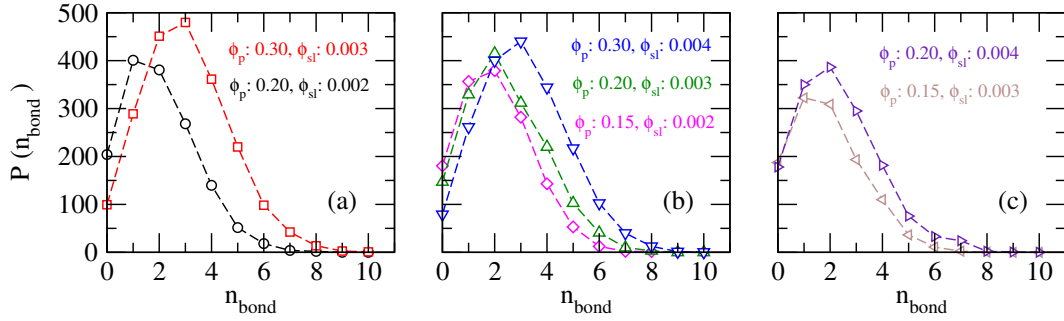


Fig. 10 Variation of the distribution of the number of particles having n_{bond} number of bonds for (a) $\phi_{sl}/\phi_p = 0.01$ (b) $\phi_{sl}/\phi_p \approx 0.013$ and (c) $\phi_{sl}/\phi_p = 0.02$.

ous case, the effect of particle fraction is observed quite distinctly. The distribution show a rightward shift with increasing particle content as well as increasing value at the peak. It can be expected that increasing the particle content (ϕ_p), while keeping the liquid content (ϕ_{sl}) constant will allow for more number of particles available for bond formation. Given the fact that not all the secondary liquid is utilised in bond formation (see fig. 7), increasing particle content will lead to more effective use of the available liquid leading to increased number of bond formation and consequently rightward shift in the distribution as well as an increase in the maximum value. The yield stress shows a monotonic increase, from 0.009 Pa to 0.13Pa in case (a), from 0.055 Pa to 0.17 Pa in case (b) and from 0.18 Pa to 0.8 Pa in case (c). This

increase in the yield stress can be attributed primarily to the increase in the number of bonds per particle with increasing ϕ_p given that ϕ_{sl} is maintained constant in each case.

The simultaneous increase in ϕ_{sl} as well as ϕ_p so as to maintain the ratio ϕ_{sl}/ϕ_p constant corresponds to vertically upward traversing in the images shown in fig. 6. The distribution for these cases is shown in fig. 10. The distribution shows a rightward shift and an increased peak value in each case. Simultaneous increase of both the entities leads to (i) large number of bonds formed per particle due to increased particle and liquid availability resulting in a qualitative change in the distribution and (ii) possible increase of liquid bridge volume due to increased liquid content. The increase in the yield stress,

from 0.025 Pa to 0.17 Pa in case (a), from 0.009 Pa to 0.8 Pa in case (b) and from 0.044 Pa to 0.35 Pa in case (c), can be attributed to contributions from both, increased number of bonds per particle and possible increase in liquid bridge volume (Weis et al., 2019).

The overall behavior of the microstructure discussed above suggests that the distribution, $P(n_{bond})$, is primarily dependent on ϕ_p and only marginally on ϕ_{sl} , whereas the yield stress shows significant dependence on ϕ_{sl} as well as ϕ_p . Further, the change in the number of bonds per particle does not seem to be the only factor that correlates with the changes in the yield stress. The data suggests that the changes in the yield stress can also occur due to possible change in the liquid bridge volume that cannot be quantified appropriately. Further, it is not possible to correlate the extent of the increase in the yield stress in every case with the distribution curves.

4 Conclusions

In this study, we have experimentally investigated the flow and structure of a capillary attractive force initiated gel using rheology and tomography techniques. The experiments were carried out for a range of particle volume fraction and varying concentration of secondary liquid which induces the necessary capillary attractive force. The rheology behavior predominantly comprises of a yield stress with a linear behavior of shear stress at high shear rates. The yield stress extracted from the flow curves shows, hitherto unobserved, highly non-linear dependence on the secondary liquid fraction and particle concentration. The dependence on the particle fraction is, however, stronger compared to that on the secondary liquid. A power-law dependence, of exponent 2, is observed for secondary liquid fraction for small enough values of ϕ_{sl}/ϕ_p , while a rapid increase is observed with increased particle volume fraction. Microstructural details of the gel have been extracted using direct visualisation in three dimensions through X-ray tomography followed by image analysis to obtain particle locations (centroids). The local porosity of the gel is observed to increase with increasing secondary liquid fraction due to more localised compaction by particle rearrangements, while it decreases with increasing particle fraction due to crowding, the yield stress increasing in both the cases. In the former case, the increase in yield stress can be attributed primarily due to increase in the liquid bridge volume and a very slight change in the number of bonds per particle. In the latter case, the yield stress seems to increase primarily due to increase in the number of bonds between particles, each contributing to capillary attractive force which needs to be overcome to initiate yielding. The above behavior is reflected reasonably well through the distributions of particle-particle bonding (or coordination number) obtained from image analysis.

The observed rheology should provide a strong impetus towards modeling of the yield stress behavior for

such gel systems. It is not quite clear whether the differences in the behavior are only due to the larger particle sizes (weaker gels) employed in this work compared to all other studies. Theoretical constitutive modeling will then, have to be formulated to encompass the qualitative change in the observed behavior across a range of particle sizes. Equally interesting and challenging would be to investigate the behavior of such gel systems for (i) spherical particles with heterogeneity in the wettability across particle surface (Janus particles) (ii) binary mixture of particles based on their wettability, one wettable with respect to primary liquid while other with respect to secondary liquid and (iii) particles with aspherical or rod-like shapes. Understanding the mechanism of gelation, structural formation, strength of the gels for such systems which are quite different than those being studied till now and which also are of much more practical relevance should form the scope of the future research work for this exciting gel forming system.

5 Supplementary material

Movies corresponding to all the images shown in fig. 6 are provided as supplementary material for ready reference. Each movie is obtained using X-ray tomography imaging over a region ($20 \times 20 \times 20$ particle diameters) by rotating the sample over 360 degrees.

Acknowledgements We thank Mahesh Tirumkudulu for insightful suggestions which helped us to improve upon the manuscript. We are also very thankful to Mr. Arun Torris for the assistance provided in tomography imaging, Mayuresh Kulkarni for assistance in laser imaging, Arun Banpurkar for providing help in measuring the surface tension of all liquids and Shankar Ghosh for assistance in refractive index measurements of all the materials. The financial support from Science & Engineering Research Board, India (Grant No. SB/S3/CE/017/2015) is gratefully acknowledged.

A Appendix

A.1 Rheology dependence on shear gap

Stress ramp measurements were performed for three combinations of particle fraction (ϕ_p) and secondary liquid fraction (ϕ_{sl}) in concentric cylinder (cup-bob) geometry with outer cylinder (cup) of two different radii, viz. 11.33 mm and 14.33 mm. This realizes two shear gaps 3 mm and 6 mm since the inner cylinder (bob) is of radius of 8.33 mm. Given the particle mean diameter of $D = 350 \pm 50$ microns, the two shearing gaps then correspond to approximately 8 – 9 and 16 – 18 particle diameters. The variation of stress versus shear rate for two shear gaps and different particle-liquid fraction combination is shown in fig. 11. The consistently smaller values of stress for the smaller gap compared to those for

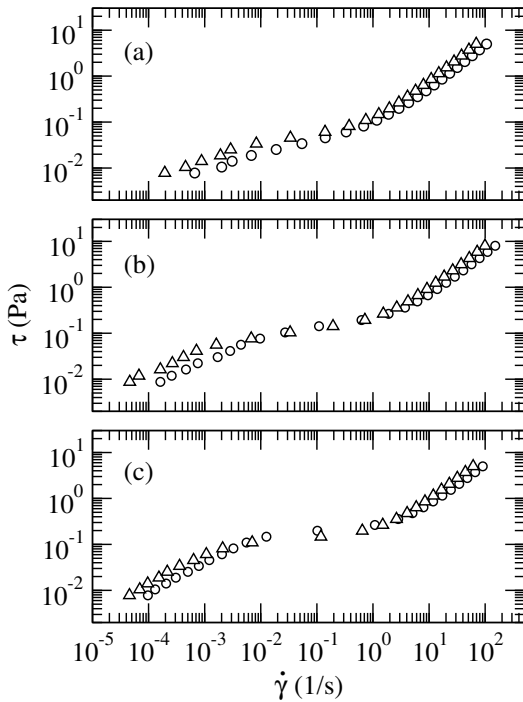


Fig. 11 Effect of shear gap on stress ramp rheology behavior. (a) $\phi_p : 0.15, \phi_{sl} : 0.002$ (b) $\phi_p : 0.20, \phi_{sl} : 0.003$ and (c) $\phi_p : 0.30, \phi_{sl} : 0.002$. Circles and triangles, respectively, represent the data acquired for shear gap of 3 mm (~ 10 particle diameters) and 6 mm (~ 20 particle diameters).

the larger gap (by a factor of 50% or less) over the entire shear rate range suggests the presence of a small amount of slip. Further, the effect of slip, even if small, seems to be more pronounced for the data below yielding. At the same time, the near similar behavior for both gaps indicate that the overall results shown for 3 mm shear gap in the main text and the conclusions drawn from them are not affected qualitatively by the presence of a small amount of slip. Moreover, the values of yield stress which is the main focus of this work remain nearly the same for both the shear gaps.

A.2 Stress strain relationship

Stress ramp rheology experiments were performed for three combinations of ϕ_p and ϕ_{sl} and for two different acquisition times, viz. $t_{aq} = 10$ seconds and $t_{aq} = 100$ seconds. The variation of the applied stress and corresponding recorded strain experienced by the sample at the end of the acquisition time is shown in fig. 12. The stress-strain data for both the acquisition time shows reasonable superimposition below the yielding, which points towards a possible elastic behavior, though the data shown in fig. 13 suggests plastic deformation. Further, the curves, above the yield point, are distinctly different for both the acquisition times suggestive of predominantly plastic deformation of the sample. The yield-

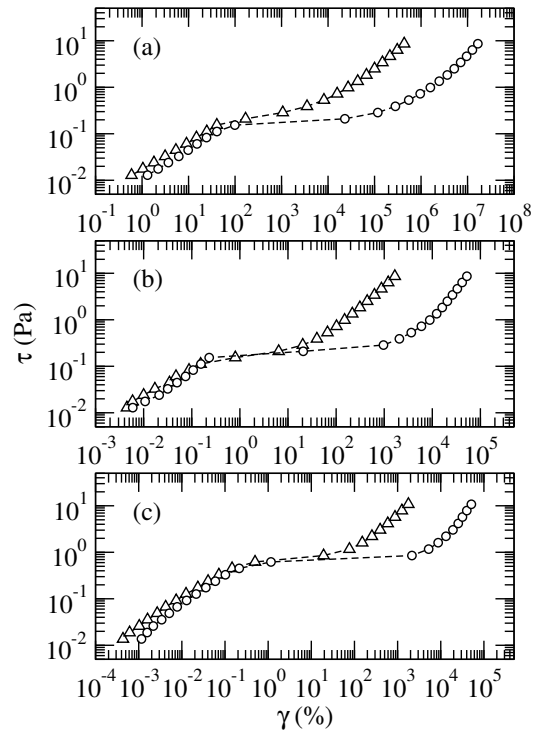


Fig. 12 Variation of shear stress with strain across the entire stress ramp change. (a) $\phi_p : 0.20, \phi_{sl} : 0.003$ (b) $\phi_p : 0.20, \phi_{sl} : 0.004$ and (c) $\phi_p : 0.30, \phi_{sl} : 0.002$. Triangles and circles, respectively, represent the data acquired for acquisition time $t_{aq} = 10$ seconds and $t_{aq} = 100$ seconds.

ing behavior, however, remains unchanged by the acquisition times as seen from the near identical yield stress for both cases. The exact mechanism of this apparent plastic as well as possible elastic deformation below yielding is not clear and will require flow imaging in the limit of low shear rates not within the scope of this work.

A.3 Time dependent strain evolution

The cumulative evolution of strain (γ) with time (t) during a step-stress ramp experiment is shown in fig. 13 for two different acquisition times (t_{aq}). Different gel samples, albeit with same $\phi_{sl} = 0.003$ and $\phi_p = 0.2$, are used to obtain data for each acquisition time. Stress was increased in step-wise manner from 0.00865 Pa to 8.65 Pa and the time interval between two consecutive stress levels was equal to the acquisition time. The data acquired with $t_{aq} = 100$ s was re-scaled by dividing time (t) by a factor of 10. This is done to enable direct comparison of the strain evolution data between the experiments with $t_{aq} = 10$ s and $t_{aq} = 100$ s. In both acquisition time experiments, the data shows a yield event in which the strain increases rapidly beyond a certain stress (or strain) level. Before the yield event the strain values are small suggestive of a solid-like behavior. However, for each level of applied stress the strain jumps slightly and

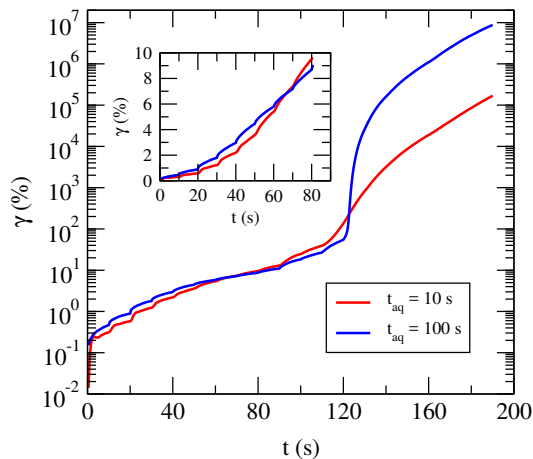


Fig. 13 Cumulative evolution of strain with time at two different acquisition time (t_{aq}) during the step-stress ramp experiment for $\phi_p : 0.2$ and $\phi_{sl} : 0.003$. The applied stress values increase in a step-wise manner from 0.00865 Pa to 8.65 Pa. Inset: Data at early times ($t < 80s$) shown on a linear scale.

then increases more slowly with time, which suggests that the material in its pre-yield stage actually creeps slowly. Thus, the pre-yield state is not truly elastic, but comprises plastic deformation to certain extent, perhaps, arising due to rearrangement of particle-particle bonds, i.e. breakage of bonds and reforming with different particles resulting in a local rearrangements. Because of the creep flow, the strain values with $t_{aq} = 100$ s are always higher than those with $t_{aq} = 10$ s. Interestingly, the sample with $t_{aq} = 10$ s tends to yield (i.e., the strain starts increasing rapidly) at a slightly lower stress value (0.162 Pa) than the sample with $t_{aq} = 100$ s which tends to yield at 0.216 Pa. The yield event for the sample with $t_{aq} = 100$ s is also more distinct than that for the sample with $t_{aq} = 10$ s. These differences are likely because the sample with $t_{aq} = 100$ s is also ageing to a greater extent during the acquisition time compared to the sample with $t_{aq} = 10$ s. Ageing probably results in stronger network, which resists yielding and also breaks more distinctly. From the behavior described above, the exact mechanism of yielding is not entirely clear. It seems that the solid-like material in the pre-yield state actually creeps slowly until it yields. However, the yield strains for both cases are not identical (about 48% strain with $t_{aq} = 10$ and about 58% with $t_{aq} = 100$ s). Further investigations of the rheology and yielding behavior of the suspension are needed which will require rheo-visualization, not within the scope of the present work.

A.4 Refractive index and density matching details

The refractive index of CHB-DEC and TG-1P liquid mixtures was measured using refractometer for varying fractions of CHB (ϕ_{CHB}) and TG (ϕ_{TG}), in their re-

spective mixtures (see figure 14a). The refractive index for CHB-DEC mixture is nearly constant with varying ϕ_{CHB} while that for TG-1P mixture shows a linear variation with ϕ_{TG} . The horizontal dashed line represents the reported value for the refractive index of PMMA. In the vicinity of this value, ϕ_{CHB} and ϕ_{TG} were varied in small increments, respectively, in CHB-DEC and TG-1P mixtures in order to determine the optimal binary composition of each mixture at which the refractive index was closest to PMMA. For each small variation, the suspension (of PMMA particles in CHB-DEC or TG-1P liquid mixture) was placed in a transparent walled rectangular cell and a thin laser line, of thickness about one-tenth that of the particle diameter, was transmitted through one of the faces of the cell, about 10 particle diameters away from the other orthogonal face of the cell. The laser line was imaged on a planar surface on the other side of the cell placed orthogonal to the incident laser line. The values of ϕ_{CHB} and ϕ_{TG} in their respective mixtures, which resulted in minimum scatter (measured as the variation of intensity with the width of the scattered image) yielded the optimal value of the liquid mixture composition (to the order of third decimal place) for each constituent. This matching is good enough to obtain near transparency upto about 20 - 30 particle diameters inside the sample.

The densities of the CHB-DEC and TG-1P liquid mixtures measured using mass-volume method are shown in figure 14b for varying ϕ_{CHB} and ϕ_{TG} , in their respective mixtures. The horizontal dashed line represents the reported value of density for PMMA (≈ 1.193). In the vicinity of this value, ϕ_{CHB} was varied (from 0.66 to 0.71) in very tiny increments (inset (c) in figure 14b). As for the refractive index matching procedure, for every small variation, the suspension of PMMA particles in CHB-DEC liquid mixture, placed in a transparent walled rectangular cell was illuminated using a thin laser line. Given the negligible variation of refractive index of CHB-DEC mixture with its composition and its closeness to the refractive index of particles, the sample is rendered nearly transparent. A small amount of fluorescent dye (Carboxy-X-rhodamine succinimidyl ester procured from Sigma-Aldrich) added to the CHB-DEC liquid mixture fluoresces a plane in the sample showing (undyed) particles in that plane as black shadows on a bright background. The negligible variation of positions of different particles in any plane over a time period of three hours provides the composition ($\phi_{CHB} = 0.686$) which matches the density of CHB-DEC mixture with that of the particle to the accuracy of three decimal places. Similar procedure (using Nile Red from Sigma Aldrich as a fluorescent dye) was followed for TG-1P mixture which yielded the composition ($\phi_{TG} = 0.865$) having the density same as the particles to the accuracy of three decimal places. Any further improvement in the accuracy is not possible due to practical limitations in varying the concentration accurately enough.

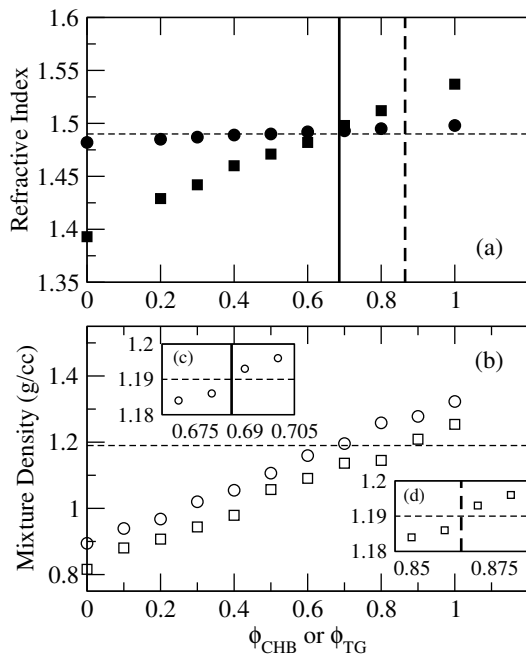


Fig. 14 Variation of the measured values of (a) refractive index and (b) density of the liquid mixture with volume fraction of one of its constituents (TG or CHB). Circles represent data for ϕ_{CHB} in its mixture with DEC. Squares represent values for ϕ_{TG} in its mixture with 1P. The horizontal dashed line in (a) and (b), respectively, represents the reported values of refractive index and density for PMMA. Inset: An expanded view of the variation of mixture density for small changes to (c) ϕ_{CHB} and (d) ϕ_{TG} in their respective mixtures. The solid vertical line in (c) represents the value of ϕ_{CHB} desired for accurate density matching, while the solid vertical line in (a) provides the closeness of refractive index matching using the same value of ϕ_{CHB} . The dashed vertical line in (d) represents the value of ϕ_{TG} desired for accurate density matching, while the dashed vertical line in (a) provides the closeness of refractive index matching using the same value of ϕ_{TG} .

It is to be noted that while the density matching composition for CHB-DEC mixture is also close to the refractive index matching composition for the same mixture (solid line in figure 14a), the same does not hold for TG-1P mixture. The density matching composition induces significant mis-match in the refractive indices between TG-1P mixture and the particles (dashed line in figure 14a). The primary importance during the gel preparation is, however, given to accurate matching of densities of liquid mixture and particles. Thus, suspensions of PMMA particles in CHB-DEC mixture of composition $\phi_{CHB} = 0.686$, which is the primary liquid, and containing tiny quantities of TG-1P mixture as the secondary liquid of composition $\phi_{TG} = 0.865$ are exactly density matched and are also transparent enough to be viewed to a depth of about 20–30 particle diameters inside the suspension. All the measurements pertaining to density and refractive index matching and laser imaging

were performed in a room with temperature maintained at 25 ± 1 deg C.

References

- Bonn D, Denn MM, Berthier L, Divoux T, Manneville S (2017) Yield stress materials in soft condensed matter. *Rev Mod Phys* 89:035005
- Bossler F, Koos E (2016) Structure of particle networks in capillary suspensions with wetting and non wetting fluids. *Langmuir* 32:1489
- Bossler F, Maurath J, Dyhr K, Willenbacher N, Koos E (2018) Fractal approaches to characterize the structure of capillary suspensions using rheology and confocal microscopy. *J Rheol* 62:183
- Cavalier K, Larchè F (2002) Effects of water on the rheological properties of calcite suspensions in dioctylphthalate. *Coll Surf A* 197:173
- Coussot P, Ancey C (1999) Rheophysical classification of concentrated suspensions and granular pastes. *Phys Rev E* 59:4445
- Danov KD, Georgiev MT, Kralchevsky PA, Radulova GM, Gurkov TD, Stoyanov SD, Pelan EG (2018) Hardening of particle/oil/water suspensions due to capillary bridges: Experimental yield stress and theoretical interpretation. *Adv Coll Int Sci* 251:80–96
- Dittmann J, Willenbacher N (2014) Micro structural investigations and mechanical properties of macro porous ceramic materials from capillary suspensions. *J Am Ceram Soc* 97:3787
- Domenech T, Velankar SS (2014) Capillary-driven percolating networks in ternary blends of immiscible polymers and silica particles. *Rheol Acta* 53:593
- Domenech T, Velankar SS (2015) On the rheology of pendular gels and morphological developments in paste-like ternary systems based on capillary action. *Soft Matter* 11:1500
- Fortini A (2012) Clustering and gelation of hard spheres induced by pickering effect. *Phys Rev E* 85:040401
- Georgiev MT, Danov KD, Kralchevsky PA, Gurkov TD, Krusteva DP, Arnaudov LN, Stoyanov SD, Pelan EG (2018) Rheology of particle/water/oil three-phase dispersions: Electrostatic vs. capillary bridge forces. *J Coll Int Sci* 513:515–526
- Heidlebaugh SJ, Domenech T, Iasella SV, Velankar SS (2014) Aggregation and separation in ternary particle/oil/water systems with fully wettable particles. *Langmuir* 30:63
- Herminghaus S (2005) Dynamics of wet granular matter. *Adv Phys* 54:221
- Joshi YM, Petekidis G (2018) Yield stress fluids and ageing. *Rheol Acta* 57:521–549
- Kao SV, Nielsen LE, Hill CT (1975) Rheology of concentrated suspensions of spheres. ii. suspensions agglomerated by an immiscible second liquid. *J Colloid Int Sci* 53:367

- Koos E (2014) Capillary suspensions: Particle networks formed through the capillary force. *Curr Opin in Coll Int Sci* 19:575
- Koos E, Willenbacher N (2011) Capillary forces in suspension rheology. *Science* 331:897
- Koos E, Willenbacher N (2012) Particle configurations and gelation in capillary suspensions. *Soft Matter* 8:3988
- Koos E, Johannsmeier J, Schwebler L, Willenbacher N (2012) Tuning suspension rheology using capillary force. *Soft Matter* 8:2620
- Koos E, Kanno W, Willenbacher N (2014) Restructuring and aging in a capillary suspension. *Rheol Acta* 53:947
- Lu PJ, Weitz DA (2013) Colloidal particles: crystals, glasses and gels. *Annu Rev Condens Matter Phys* 4:217
- McCulfor J, Himes P, Anklam MR (2011) The effects of capillary forces on the flow properties of glass particle suspensions in mineral oil. *AIChE J* 57:2334
- Mitsoulis E (2007) Flows of viscoplastic materials: models and computations. *Rheology Rev* p 135
- Moller P, Fall A, Chikkadi V, Derks D, Bonn D (2009) An attempt to categorize yield stress fluid behavior. *Phil Trans R Soc A* 367:5139–5155
- Papanastasiou TC (1987) Flow of materials with yield. *J Rheol* 31:385
- Pietsch WB, Rumpf H (1967) Adhesion, capillary pressure, liquid volume and angle of contact of a liquid bridge between two spheres. *Chem Ing Tech* 39:885
- Pitois P, Moucheron P, Chateau X (2000) Liquid bridge between two moving spheres: An experimental study of viscosity effects. *J Colloid Int Sci* 231:26
- Roy S, Tirumkudulu M (2016) Universality in consolidation of colloidal gels. *Soft Matter* 12:9402
- Scheel M, Seemann R, Brinkmann M, Michiel MD, Sheppard A, Breidenbach B, Herminghaus S (2008) Morphological clues to wet granular pile stability. *Nat Mat* 7:189–193
- Schubert H (1984) Capillary forces - modelling and application in particle technology. *Powder Technol* 37:105
- Stickel JJ, Powell RL (2005) Fluid mechanics and rheology of dense suspensions. *J Fluid Mech* 37:129
- Strauch S, Herminghaus S (2012) Wet granular matter: a truly complex fluid. *Soft Matter* 8:8271
- Weis S, Schroder-Turk GE, Schroter M (2019) Structural similarity between dry and wet sphere packings. *New J Phys* 21:043020
- Willet CD, Adams MJ, Johnson SA, Seville JPK (2000) Capillary bridges between two spherical bodies. *Langmuir* 16:9396
- Yang J, Velankar SS (2017) Preparation and yielding behavior of pendular network suspensions. *J Rheol* 61:217–228